Journal of
Mechanics of
Materials and Structures

MULTIMODAL PIEZOELECTRIC DEVICE FOR ENERGY HARVESTING FROM ENGINE VIBRATION

Claudio D. Gatti, José M. Ramirez, Mariano Febbo and Sebastián P. Machado

Volume 13, No. 1 January 2018

msp

JOURNAL OF MECHANICS OF MATERIALS AND STRUCTURES
Vol. 13, No. 1, 2018
dx.doi.org/10.2140/jomms.2018.13.17

MULTIMODAL PIEZOELECTRIC DEVICE FOR ENERGY HARVESTING FROM ENGINE VIBRATION

CLAUDIO D. GATTI, JOSÉ M. RAMIREZ, MARIANO FEBBO AND SEBASTIÁN P. MACHADO

In a conventional transport vehicle, only about 10% to 16% of the energy from the fuel is used to move it down the road. The rest of the energy is lost in the brakes, transmission, engine, accessories, rolling resistance, aerodynamic drag, and idle losses. Among all of these, the largest loss is the energy lost in the engine (approximately 63%), which is mostly wasted as vibration. Our work develops an energy harvesting device that is capable of collecting energy for different gear ratios in a car. For this reason, the structural design is oriented to create a harvesting structure with several resonant modes in a frequency bandwidth between 1600 rpm–4600 rpm, which was the range obtained through driving tests in a conventional diesel car. The harvesting device is based on a piezoelectric fiber composite beam with a high fatigue resistance placed in the middle of two mass-spring systems, which provide the multimodal character of the device. A one-dimensional analytical model based on a Lagrangian formulation is used to predict the dynamical behavior of the device. The equations provide a very good quantitative description of the system, which is also modeled with a three-dimensional finite element code (Abaqus) for numerical validation. Experimental tests are then carried out and compared with theoretical findings. The results show a very good agreement between both of them, revealing the multimodal nature of the device in the operating bandwidth, with a significant output power for different engine speeds, sufficient to feed low-power monitoring wireless systems.

1. Introduction

Energy harvesting is a subject of great importance in the scientific world. In the area of transport vehicles (land, sea, or air) that use combustion engines for propulsion, fuel consumption involves two main drawbacks. Firstly, there is environmental contamination and thus degradation of the ozone layer due to the emission of polluting gases from the incomplete combustion of fuel. From this point of view, reducing its consumption implies a reduction of greenhouse gases, and thus less damage to the atmosphere. Secondly, fossil fuels are nonrenewable natural resources. This means that in the near future there will be a fuel shortage if current consumption trends continue. In this context, it is important to implement energy harvesting techniques in order to minimize these drawbacks [Xiao and Wang 2014].

Energy harvesting can be obtained from solar, wind, tidal, kinetic, thermal sources, or mechanical vibrations, the latter being the object of study of this work. After the source has been defined, the energy can be recovered through electromagnetic devices, thermoelectric, or piezoelectric materials [IEE 1988; Erturk and Inman 2011], among others.

The use of piezoelectric materials that take advantage of mechanical deformations caused by vibration is of great interest for generating an electric potential difference. Piezoelectric materials have been used

Keywords: piezoelectric materials, vehicles, engines, vibrations, system recovery.

in different device variants, such us axial cymbals [Kim et al. 2004; 2006; Ren et al. 2010], corrugated piezoelectric springs [Harne 2013], linear [Ramirez et al. 2017; Van Blarigan et al. 2015] and nonlinear piezoelectric beams [Harne and Wang 2013], aeroelastic systems [He and Gao 2013; Bibo and Daqaq 2013], and multilayer stacks [Xu et al. 2013]. Most of them are designed to work at resonance, where the system is capable of recovering maximum energy due to the large deformations in the piezoelectric material. The main disadvantage of this approach is that the systems are efficient for a single excitation frequency (single-mode generation), which has to be coincident with one of the natural frequencies of the harvesting device. As soon as the excitation frequency moves away from this condition (off-resonance condition), the generated voltage drops abruptly. With the intention of overcoming this situation, more sophisticated proposals of energy harvesting devices have implemented multimodal systems in order to have multiple resonant modes in the range of possible excitation frequencies [Sadeqi et al. 2015; Zhu et al. 2010; Rezaei-Hosseinabadi et al. 2016].

In the industry of transport vehicles, various energy harvesting devices have been used mainly to feed low-power wireless transmitters. Some of the most important works are based on rotational energy [Roundy 2008; Wang et al. 2010; 2013] or deformation of the tires [Lee et al. 2012]. Another important issue is energy recovery by means of the vehicle's suspension dampers [Zhang et al. 2007; 2012; Zuo and Zhang 2013], where a large amount of energy can be collected. However, there are few works that consider energy recovery from engine vibration. For example, Glynne-Jones et al. [2004] proposed an electromagnetic microgenerator mounted on the top of the engine block of a car with an average generation of 157 μW. Therefore, the possibility of harvesting energy from engine vibrations using a piezoelectric generator is addressed in this paper.

There are several different issues that can be explored for developing this investigation. We will focus on the two that we consider central in this case:

(a) the recovery of the maximum possible energy over a well-defined bandwidth, and

(b) the long fatigue life of the piezoelectric beams.

Our proposal attempts to give a solution to these important problems. For the first issue, we propose a multimodal system with multiple resonant modes in a well-defined range of frequencies. This operating bandwidth will be defined by making a drive test in a conventional car in our city at normal speed. For the second issue, we will use a composite beam of interdigitated electrodes and piezoelectric fibers of PZT-5A [Nelson et al. 2003; Beckert and Kreher 2003; Bowen et al. 2006; Hareesh et al. 2012; Lin et al. 2013] as the harvesting device. The selected piezofiber composite has significant advantages over other conventional piezoelectric sheets. Firstly, the longitudinally oriented piezofibers give large flexibility to the sheets, and thus long fatigue life, which enables large strains and therefore more power generation [Beckert and Kreher 2003]. Secondly, the electric field is established in the longitudinal direction due to the arrangement of the interdigitated electrodes. This makes the power generation with piezoelectric charge coefficient d_{33} (polarization in same direction of stress applied) being larger than with piezoelectric charge coefficient d_{31} (polarization in perpendicular direction of stress applied) [Uchino 1997].

Considering these preliminary issues, the paper is organized as follows. In the first section, the one-dimensional structural model together with the electromechanical Lagrange's equation and their solutions are sketched. In Section 2 we define the design parameters of the harvester and perform a computational validation of the results of the first section. In Section 3, details of the experimental tests and a comparison

between analytical and experimental voltage measurements are presented. Finally, some conclusions are drawn to show the advantages of the proposed system.

2. Dynamical modeling and electromechanical equations

Figure 1, left, shows the proposed device, which consists of a composite beam with two mass-spring systems at the ends of the beam that provide the appropriate boundary conditions. By means of this model, it is possible to modify the multimodal response by varying the parameters such as the masses and springs. The composite beam consists of a central stainless steel structure with two piezoelectric fiber composites (PFCB-W14 from Advanced Cerametrics Inc.) attached to the upper and lower surfaces (see Figure 1, right). Both piezofiber composites are connected in parallel constituting a bimorph electric system. The only thing the device is subjected to is the base excitation provided by the vehicle's engine, generating a voltage difference between the electrodes of the bimorph. In Figure 1, left, $g(t)$ is the temporal base excitation, L is the length of the composite beam, $m_{1,2}$ are the masses, $k_{1,2}$ are respectively the vertical stiffnesses of the springs at the ends $x = 0$ and $x = L$, and $k_{t1,t2}$ are respectively the torsional stiffnesses of the springs at the ends $x = 0$ and $x = L$. In Figure 1, right, b_p, h_p, b_s and h_s are the width and thickness of the piezofiber composite, and the width and thickness of the stainless steel structure, respectively.

2.1. ***Electromechanical model of the system.*** The beam is modeled according to the Bernoulli–Euler formulation [Rao 2007], considering only the vertical displacement. A Lagrangian approach [Meirovitch and Parker 2010] was used to build the system of differential equations. In the following description, the x, y, and z shown in Figure 1 correspond to axes 1, 2, and 3, respectively. The idea is to have an analytical model that allows the simple dimensioning of the multimodal device according to the range of interests that will be defined later.

The vector form of the displacement field is defined (disregarding the axial displacement and including the temporal base excitation) as

$$\boldsymbol{u} = [u_x \; u_y \; u_z]^t = [-z\partial w(x,t)/\partial x \; 0 \; w(x,t) + g(t)]^t, \tag{1}$$

where $w(x,t)$ is the transverse displacement of the neutral axis at point x and time t.

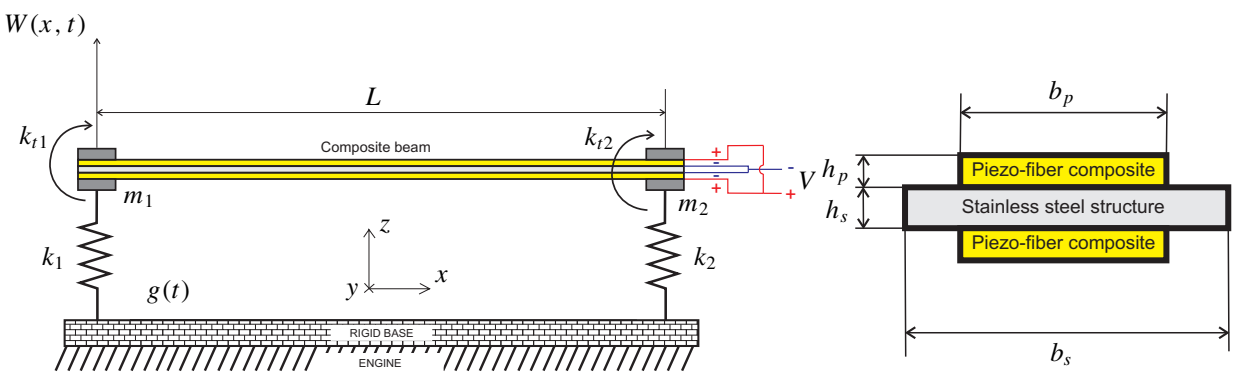

Figure 1. Harvester device. Left: scheme of the system model. Right: cross-sectional view of composite beam.

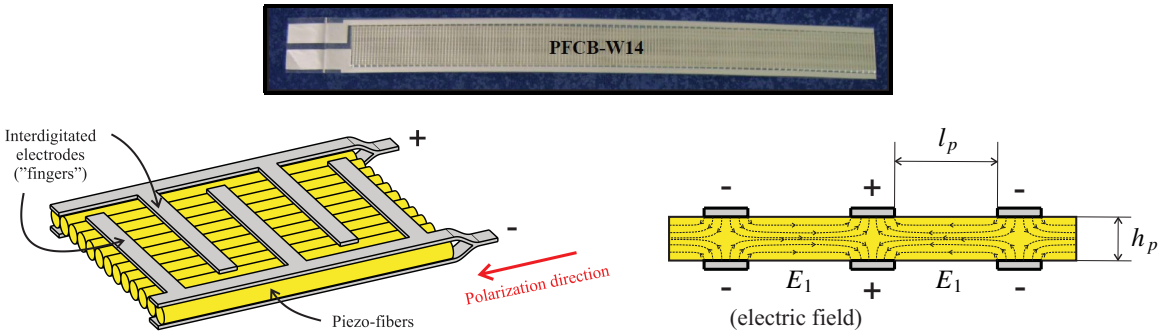

Figure 2. Schematic view of the piezofibers composite. Top: real piezofiber composite PFCB-W14 from Advanced Cerametrics Inc. (168 fingers). Left: geometric detail of only four "fingers" of the electrodes. Right: cross-sectional view of the fibers and electrodes showing the generated electric field.

The longitudinal strain is given by

$$\varepsilon_{11} = \frac{\partial u_x}{\partial x} = -z\frac{\partial^2 w(x,t)}{\partial x^2}. \tag{2}$$

From Hooke's law, the stress generated in the steel structure is

$$\sigma_{11}^s = E_s\varepsilon_{11} = -E_s z\frac{\partial^2 w(x,t)}{\partial x^2}, \tag{3}$$

where E is the Young's modulus of the substructure (steel beam). Based on the constitutive equation of the piezoelectric material [IEE 1988], and considering only the x component of the electric field, then

$$\sigma_{11}^p = E_p\varepsilon_{11} - \bar{e}_{11}E_1 = -E_p z\frac{\partial^2 w(x,t)}{\partial x^2} - \bar{e}_{11}E_1, \tag{4}$$

where $\bar{e}_{11} = d_{11}E_p$ is a piezoelectric constant and E_p is the Young's modulus of the piezoelectric sheet. Furthermore, the electric field generated in the longitudinal direction E_1 can be modeled with sufficient accuracy by [Nelson et al. 2003]

$$E_1 = -\frac{v_C(t)}{l_p}, \tag{5}$$

with l_p being the distance in the x direction between the fingers of the positive and negative electrodes of each piezofiber composite (see Figure 2).

Now, the total potential energy of the system U is the sum of the potential energy of the beam U_b and springs U_{k1} and U_{k2}. i.e., $U = U_b + U_{k1} + U_{k2}$. Thus, the expression of the potential energy of the beam is given by [Erturk and Inman 2011]

$$U_b = \frac{1}{2}\left(\int_{V_s} \boldsymbol{\varepsilon}^t\boldsymbol{\sigma}\,\mathrm{d}V_s + \int_{V_p} \boldsymbol{\varepsilon}^t\boldsymbol{\sigma}\,\mathrm{d}V_p\right). \tag{6}$$

The first and the second volume integrals within the parentheses of (6) concern the steel structure and the piezoelectric element, respectively.

symbol	quantity	value
A_s	cross sectional area of the steel structure	$b_s h_s$
A_p	cross sectional area of the piezoelectric element[a]	$2b_s h_s$
I_s	moment of inertia of the steel structure	$\frac{1}{12}(b_s h_s^3)$
I_p	moment of inertia of the piezoelectric element[a]	$b_p h_p\left(\frac{2}{3}h_p^2 + h_p h_s + \frac{1}{2}h_s^2\right)$
J_p	coupling coefficient[a]	$[\bar{e}_{11} b_p h_p (h_p + h_s)]/l_p$
C_p	internal capacitance of the piezoelectric element[a]	$(2nb_p h_p \bar{\varepsilon}_{11}^{\varepsilon})/l_p$

[a]Totals for the entire beam (bimorph) connected in parallel.

Table 1. Geometric and electrical coefficients.

Developing the above equation yields

$$U_b = \frac{1}{2} EI \int_0^L \left(\frac{\partial^2 w(x,t)}{\partial x^2}\right)^2 \mathrm{d}x - \frac{1}{2} J_p v_C(t) \int_0^L \frac{\partial^2 w(x,t)}{\partial x^2}\,\mathrm{d}x, \tag{7}$$

where J_p is the electromechanical coupling coefficient, $EI = E_s I_s + E_p I_p$ is the flexural rigidity of the entire beam, and I_s and I_p are the cross-sectional area moments of inertia of the structure and the piezoelectric element, respectively. The calculated expressions for these geometric ratios are shown in Table 1.

Considering the vertical and torsional deformation, the elastic potential energy of the springs becomes

$$U_{ki} = \frac{1}{2}\left[k_i w(x_j,t)^2 + k_{ti}\frac{\partial w(x_j,t)^2}{\partial x}\right], \quad i = 1,2, \quad x_j = 0, L, \tag{8}$$

where k_i are the vertical stiffnesses and k_{ti} are the torsional stiffnesses of the springs.

Similarly, the total kinetic energy of the system T is the sum of the kinetic energy of the beam T_b and end masses T_{m1} and T_{m2}, i.e., $T = T_b + T_{m1} + T_{m2}$. Thus, the kinetic energy of the beam is [Erturk and Inman 2011]

$$T_b = \frac{1}{2}\left(\int_{V_s} \rho_s \frac{\partial \boldsymbol{u}^t}{\partial t}\frac{\partial \boldsymbol{u}}{\partial t}\,\mathrm{d}V_s + \int_{V_p} \rho_p \frac{\partial \boldsymbol{u}^t}{\partial t}\frac{\partial \boldsymbol{u}}{\partial t}\,\mathrm{d}V_p\right), \tag{9}$$

where ρ_s and ρ_p represent the mass density of the steel and the piezoelectric element, respectively. After some algebra, (9) reads

$$T_b = \tfrac{1}{2}\rho A \int_0^L \left[\frac{\partial w(x,t)^2}{\partial t} + 2\frac{\partial w(x,t)}{\partial t}\dot{g}t + \dot{g}(t)^2\right]\mathrm{d}x, \tag{10}$$

where $\rho A = \rho_s A_s + \rho_p A_p$ is the mass per unit length of the beam, and A_s and A_p are the cross-sectional areas of the steel structure and the piezoelectric sheet, respectively (see Table 1).

Taking into account the rotational inertia and vertical movement, the kinetic energy of the masses becomes

$$T_{mi} = \tfrac{1}{2}m_i\left[\frac{\partial w(x_i,t)^2}{\partial t} + 2\frac{\partial w(x_i,t)}{\partial t}\dot{g}(t) + \dot{g}(t)^2\right] + \tfrac{1}{2}J_i\left(\frac{\partial^2 w(x_i,t)}{\partial t\,\partial x}\right)^2, \quad i=1,2,\ x_1=0,\ x_2=L. \tag{11}$$

The equivalent electric circuit for the PFCB-W14 piezofiber composite used in this work is schematically shown in Figure 3. It consists of a current generator and two capacitive-resistive impedances

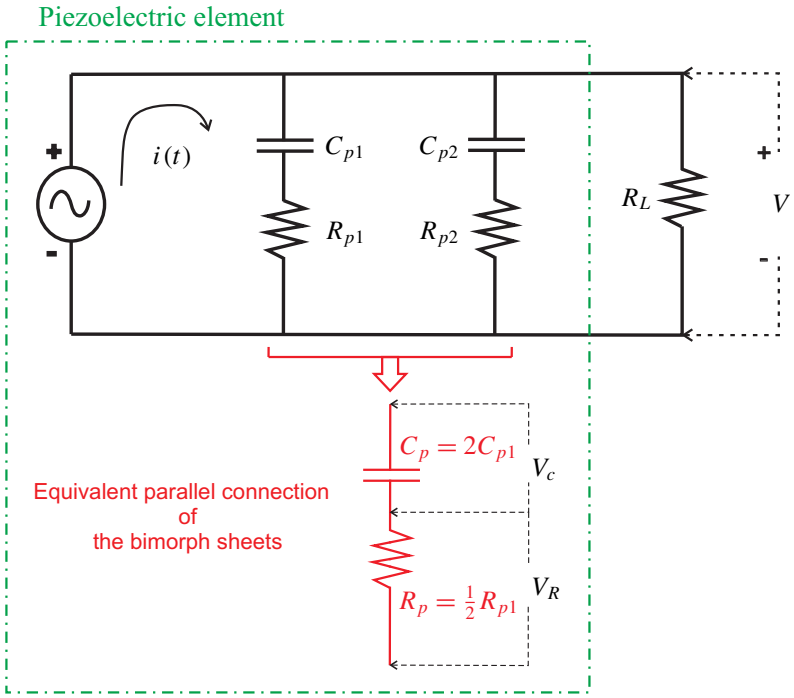

Figure 3. Equivalent electrical circuit of the PFCB-W14 piezofiber composite bimorph.

($C_{p1,2}$-$R_{p1,2}$) connected in parallel, representing each piezoelectric sheet. In practical situations, the output voltage is rectified and conditioned by a DC-DC converter, for example, to store the power in a battery or a supercapacitor. However, a resistive load resistance R_L is added here as an output load in order to easily calculate the output power, which has been previously used in similar works by other authors [Erturk and Inman 2011; Ramirez et al. 2017].

In order to compute the electric potential energy, we must take into account its integral representation as expressed in [Erturk and Inman 2011]:

$$W_{ie} = \frac{1}{2}\int_{V_p} E_1 D_1 \, \mathrm{d}V_p, \tag{12}$$

where the electric displacement is defined from the linear constitutive equation for piezoelectric materials as $D_1 = \bar{e}_{11}\varepsilon_{11} + \bar{\varepsilon}^{\varepsilon}_{11} E_1$ [IEE 1988], with $\bar{\varepsilon}^{\varepsilon}_{11}$ being the permittivity of the piezoelectric sheet at constant strain.

The expression for the electric power is obtained by using D_1 and E_1 as

$$W_{ie} = \tfrac{1}{2} n J_p v_C(t) \int_0^{l_p} \frac{\partial^2 w(x,t)}{\partial x^2} \, \mathrm{d}x + \tfrac{1}{2} C_p v_C(t)^2, \tag{13}$$

where C_p (see Table 1) is the total internal capacitance of both piezoelectric sheets (connected in parallel) as shown in Figure 3.

position	shear $(E_sI_s + E_pI_p)\phi_i'''(x)$	moment $(E_sI_s + E_pI_p)\phi_i''(x)$
at 0	$\phi_i(x)(m_1\omega^2 - k_1)$	$\phi_i'(x)(k_{1t} - J_1\omega^2)$
at L	$\phi_i(x)(k_2 - m_2\omega^2)$	$\phi_i'(x)(J_2\omega^2 - k_{t2})$

Table 2. Boundary conditions.

The damping of the system is modeled using the Rayleigh dissipation function [Mohammad et al. 1995], whose full expression R is the sum of the energy dissipation of the beam R_b and springs R_{k1} and R_{k2}, i.e., $R = R_b + R_{k1} + R_{k2}$. Considering a modal damping coefficient for the beam $r_b = 2\xi_i m_b \omega_{ni}$, where ξ_i is the modal damping ratio, $m_b = \rho AL$ is the mass of the entire beam, and ω_{ni} is its natural frequency of the i-th vibration mode, then the final expression for the dissipation of the beam, after integrating the mass density in the total volume, is

$$R_b = \xi_i \omega_{ni} \rho A \int_0^L \frac{\partial w(x,t)^2}{\partial t}\, \mathrm{d}x. \tag{14}$$

In this work, we decided to neglect the damping in the springs and attribute the total dissipation to the beam, yielding $R = R_b$.

2.2. ***Spatial discretization of the energy equations and electromechanical Lagrange equations.*** One of the commonly used procedures to obtain an analytical solution to Lagrange's equation is by the spatial discretization of the energy equations and Rayleigh dissipation function by applying the standard modal expansion method to the separation of variables [Weaver Jr. et al. 1990]. In this method, the deflection of the beam is represented as a finite sum of N generalized temporal displacements $q_i(t)$ and normalized mode shape functions $\phi_i(x)$:

$$w(x,t) = \sum_{i=1}^{N} \phi_i(x) q_i(t). \tag{15}$$

Mode shape functions, which satisfy the boundary conditions presented in Table 2, are given by

$$\phi_i(x) = C_1 \cos(\beta_i x) + C_2 \cosh(\beta_i x) + C_3 \sin(\beta_i x) + C_4 \sinh(\beta_i x), \tag{16}$$

where the eigenvalues β_i are related to the respective natural frequencies by

$$\omega_{ni} = (\beta_i L)^2 \sqrt{\frac{EI}{\rho A L^4}}. \tag{17}$$

Constants C_1, C_2, and C_3 are obtained from the boundary conditions, and C_4 is obtained from mass-normalized modal shape functions.

Finally, by applying Lagrange's formulation, the following equations are obtained:

$$\frac{\mathrm{d}}{\mathrm{d}t}\left(\frac{\partial T}{\partial \dot{q}_i}\right) + \frac{\partial U}{\partial q_i} + \frac{\partial R}{\partial \dot{q}_i} - \frac{\partial W_{ie}}{\partial q_i} = 0, \tag{18}$$

$$\frac{\partial U}{\partial v} - \frac{\partial W_{ie}}{\partial v} = Q_e, \tag{19}$$

where Q_e is the electrical charge whose time derivative gives the electrical current as $\dot{Q}_e = v(t)/R_L$.

After replacing U, T, W_{ie}, and R into (18) and (19), and deriving (19) with respect to time, two matrix equations are obtained that give the electromechanical behavior of the system:

$$\boldsymbol{M}\ddot{\boldsymbol{q}} + \boldsymbol{R}\dot{\boldsymbol{q}} + \boldsymbol{K}\boldsymbol{q} - \tilde{\boldsymbol{\theta}} v_C = \boldsymbol{f}, \tag{20}$$

$$C_p \dot{v}_c + \frac{v}{R_L} + \tilde{\boldsymbol{\theta}}^t \dot{\boldsymbol{q}} = 0. \tag{21}$$

In (20) the mass, damping, and stiffness matrices are defined as

$$\boldsymbol{M} = \begin{bmatrix} m_{11} & \cdots & 0 \\ \vdots & \ddots & \vdots \\ 0 & \cdots & m_{NN} \end{bmatrix}, \tag{22}$$

where

$$m_{ii} = \rho A \int_0^L \phi_i \phi_j \, \mathrm{d}x + m_1 \phi_i(0)\phi_j(0) + J_1 \phi_i'(0)\phi_j'(0) + m_2 \phi_i(L)\phi_j(L) + J_2 \phi_i'(L)\phi_j'(L), \tag{23}$$

$$\boldsymbol{R} = \begin{bmatrix} r_{11} & \cdots & 0 \\ \vdots & \ddots & \vdots \\ 0 & \cdots & r_{NN} \end{bmatrix}, \tag{24}$$

with

$$r_{ii} = 2\xi_i \omega_{ni} \rho A \int_0^L \phi_i \phi_j \, \mathrm{d}x + r_1 \phi_i(0)\phi_j(0) + r_2 \phi_i(L)\phi_j(L), \tag{25}$$

$$\boldsymbol{K} = \begin{bmatrix} k_{11} & \cdots & 0 \\ \vdots & \ddots & \vdots \\ 0 & \cdots & k_{NN} \end{bmatrix}, \tag{26}$$

where

$$k_{ii} = EI \int_0^L \phi_i'' \phi_j'' \, \mathrm{d}x + k_1 \phi_i(0)\phi_j(0) + k_{1t} \phi_i'(0)\phi_j'(0) + k_2 \phi_i(L)\phi_j(L) + k_{2t} \phi_i'(L)\phi_j'(L). \tag{27}$$

The electromechanical coupling vector and force vector are

$$\tilde{\boldsymbol{\theta}} = [\theta_1 \ \cdots \ \theta_N]^t, \tag{28}$$

with

$$\theta_i = J_p[\phi_i'(L) - \phi_i'(0)], \tag{29}$$

$$\boldsymbol{f} = [f_1 \ \cdots \ f_N], \tag{30}$$

where $f_i = -\sigma_i \ddot{g}(t)$ and $\sigma_i = \rho A \int_0^L \phi_i \, \mathrm{d}x + m_1 \phi_i(0) + m_2 \phi_i(L)$.

To solve (20) and (21), a harmonic base excitation [Meirovitch and Parker 2010] is proposed in the form of $g(t) = W_0 e^{i\omega t}$, with W_0 being the semiamplitude of the displacement of the base.

Now, assuming a harmonic dependence of all the variables,

$$\boldsymbol{q} = \boldsymbol{Q}e^{i\omega t}, \tag{31}$$

$$v_C = V_C e^{i\omega t}, \tag{32}$$

$$v = V e^{i\omega t}, \tag{33}$$

and using $V_C = V$, the modal displacement vector Q is obtained after replacing (31)–(33) into (20) and (21):

$$\boldsymbol{Q} = \boldsymbol{\Gamma}^{-1}\boldsymbol{F}, \tag{34}$$

where $\boldsymbol{F} = -\boldsymbol{\sigma}\omega^2 W_0$ is obtained from f_i and $g(t)$, and $\boldsymbol{\Gamma}$ results in

$$\boldsymbol{\Gamma} = -\omega^2\boldsymbol{M} + i\omega\boldsymbol{R} + \boldsymbol{K} + i\omega\left[i\omega C_p\left(\frac{R_p}{R_L}+1\right)+\frac{1}{R_L}\right]^{-1}\tilde{\boldsymbol{\theta}}\tilde{\boldsymbol{\theta}}^t. \tag{35}$$

Finally, after obtaining the modal displacements and making use of (21) and (31)–(33), the final expression for the complex voltage applied to the load resistance R_L is

$$V = -i\omega Z_{eq}\tilde{\boldsymbol{\theta}}^t\boldsymbol{Q}, \tag{36}$$

where $Z_{eq} = (i\omega C_p + 1/R_l)^{-1}$ is the equivalent impedance of the entire electrical circuit model.

It is useful to present the results in the form of power for practical comparisons. In this case, the electric power in the load resistance is simply computed as

$$P = \frac{V^2}{R_L}. \tag{37}$$

3. Harvester design and computational validation

Prior to setting the experimental tests for the harvesting device, we decided to develop a three-dimensional computer model to validate the proposed analytical approach. The selection of the masses and spring sizes of the harvester, which represent its main parameters and determine its natural frequencies, were calculated from a drive test in a car on the streets of our home city of Bahía Blanca. In this way, it was possible to observe the most frequent range of engine revolutions of the car in order to determine the range of frequencies in its normal operating mode.

The test was carried out with a four-stroke Citröen C4 Diesel 1.6 HDi instrumented with a Firelog Extreme Microtex GPS data acquisition system.

Figure 4 shows the route of the drive (upper figure) and the measured working range, rpm vs. time (lower figure). Taking into account that in the case of four-stroke engines the excitation frequency is twice the rotation of the engine [Lin and Ding 2013], the spring-mass systems for the beam ends were computed with the mechanical parameters presented in Table 3. In order to do this calculation, we made the natural frequencies of this multimodal device to be inside the bandwidth defined by Figure 4.

Once the parameters of the harvester were defined, the computational model was developed using Abaqus simulation software. The finite element mesh can be observed in Figure 5. In the model, 15400 eight-node piezoelectric linear brick elements (C3D8E) were used for the piezoelectric sheets, 26477 ten-node quadratic tetrahedron elements (C3D10) for springs, and 8892 eight-node linear brick elements

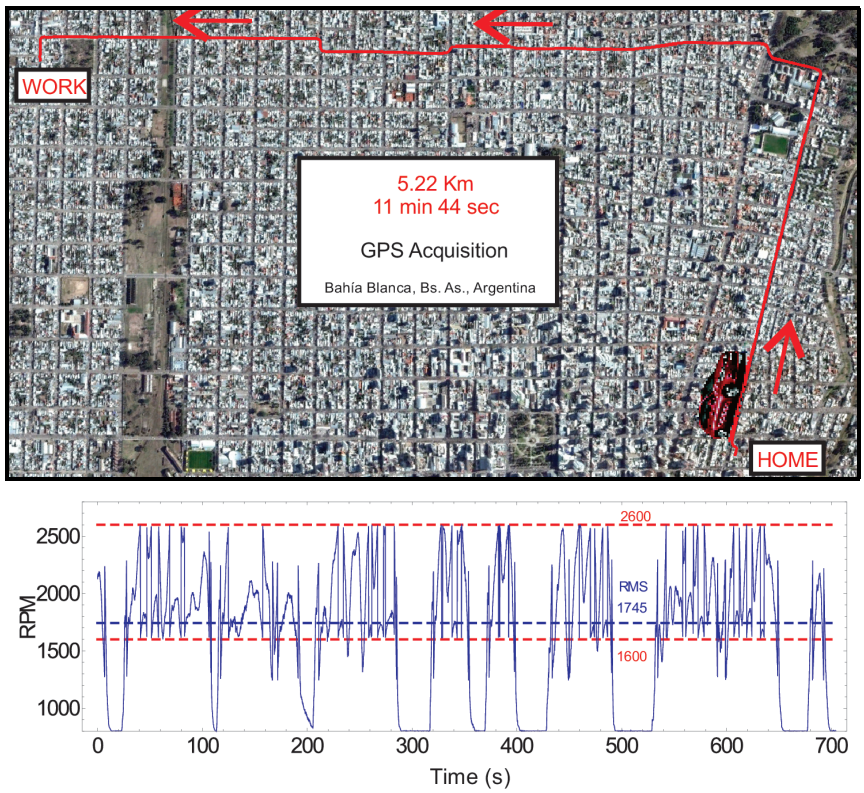

Figure 4. Rpm vs. time of a Citröen C4 engine for a short city drive.

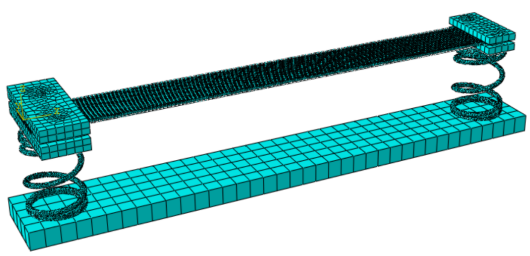

Figure 5. Abaqus 3D model of the harvesting device.

(C3D8R) for the rest of the steel parts. The test was performed in a single-step frequency mode, extracting the first seven vibrational modes. A list of the numerical values used in the calculations is presented in Tables 4 and 5.

Figure 6, left, shows a comparison between the first three flexural mode shapes obtained with analytical and Abaqus calculations. In all three cases, a very good agreement between our proposed one-dimensional model and the three-dimensional finite element method is observed. As it was one of the main objectives of the mechanical design, the first two frequencies (73 Hz and 92 Hz) are within the range of major use of the engine in the city drive.

	description	value	unit
m_1	mass at $x = 0$	19.1	gr
m_2	mass at $x = L$	6.09	gr
J_1	rotational inertia[a] at $x = 0$	3.35×10^{-7}	$\mathrm{kg \cdot m^2}$
J_2	rotational inertia[a] at $x = L$	5.86×10^{-8}	$\mathrm{kg \cdot m^2}$
k_1	vertical stiffness[b] at $x = 0$	5460	N/m
k_2	vertical stiffness[b] at $x = L$	3847	N/m
k_{t1}	flexural stiffness[b] at $x = 0$	0.68	$\mathrm{N \cdot rad/m}$
k_{t2}	flexural stiffness[b] at $x = L$	1.20	$\mathrm{N \cdot rad/m}$

[a]Of the mass at the ends.

[b]Of the spring at the ends.

Table 3. Mechanical parameters.

	description	steel structure	piezoelectric element
b	width (mm)	12.7	10.3
h	thickness (mm)	0.4	0.4
ρ	density ($\mathrm{kg/m^3}$)	8035	3750
E	Young's modulus (GPa)	180	15.2
L	length (mm)	125	125

Table 4. Numerical parameters of the beam.

	description	value	unit
d_{11}	piezoelectric charge constant	375	pm/V
$\bar{\varepsilon}_{11}^{\varepsilon}$	electrical permittivity	13.1	nF/m
R_l	load resistance	248	kΩ
C_p	internal capacitance	56.79	nF
l_p	"finger" length	0.32	mm
n	number of "fingers"	168	–

Table 5. Electrical parameters.

Figure 6, right, presents the 3D flexural mode shapes from the finite element method, together with the values of speed and gear transmission where these modes can be excited [Shigley 1972]. It is possible to observe that each natural mode is excited for many velocities or gear ratios except the third mode. This clearly demonstrates the ability of the proposed device to be in resonance for a large set of speeds.

4. Experimental validation and results

In this section, experimental tests are carried out to validate the numerical and simulation results obtained in Section 3. Figure 7, top, shows the experimental setup, consisting of a function generator (Rigol

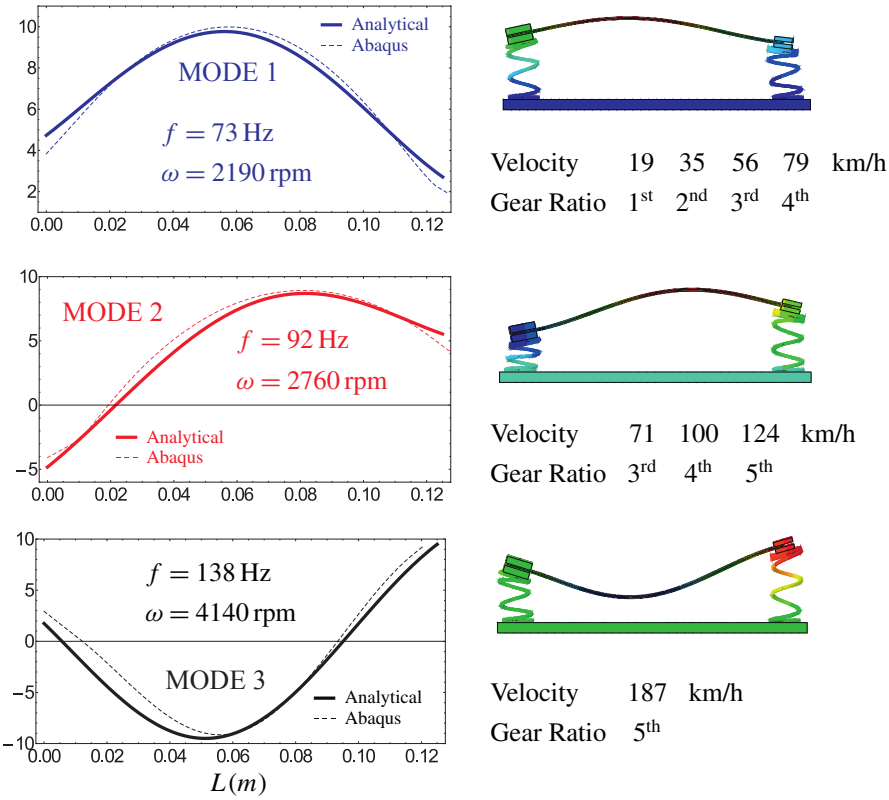

Figure 6. First three flexural mode shapes: comparison between the analytical and computational models.

DG4062) connected to a signal amplifier feeding a shaker, which excites the base of the device by variable acceleration. This acceleration signal is measured using a Wilcoxon Research 780C accelerometer, which is connected, together with the output voltage of the harvester, to a Pasco Science Workshop 750 data acquisition interface. A picture of the device is presented in Figure 7, bottom. In this last figure, the boundary conditions of the composite beam are shown in detail, where the construction method of the mass-spring systems can be observed.

Experimental data are then measured by performing a frequency sweep from 30 Hz to 180 Hz over 60 seconds. During this time interval, the accelerometer data and the piezoelectric voltage are recorded and their fast Fourier transform (FFT) are computed in order to obtain the voltage/acceleration frequency response functions in V/G units (G = gravity acceleration). The frequency is sweep up and down verifying the linear behavior of the device. The results for a load resistance of 248 kΩ and a peak base acceleration of $0.3G$ are shown in Figure 8. This selected value of the load resistance is due to a limitation of ±5 V in the input voltage of the data acquisition board. As it can be observed, the experiments and theoretical results agree reasonably well for the peaks at 73 Hz (51 V/G) and 140 Hz (15 V/G), which correspond to the first and third analytically predicted vibration modes (second and fifth experimental modes), but not so well for the second peak. In the latter case, the analytical model predicts a more conservative scenario along with a shift in frequency between the analytical and experimental values.

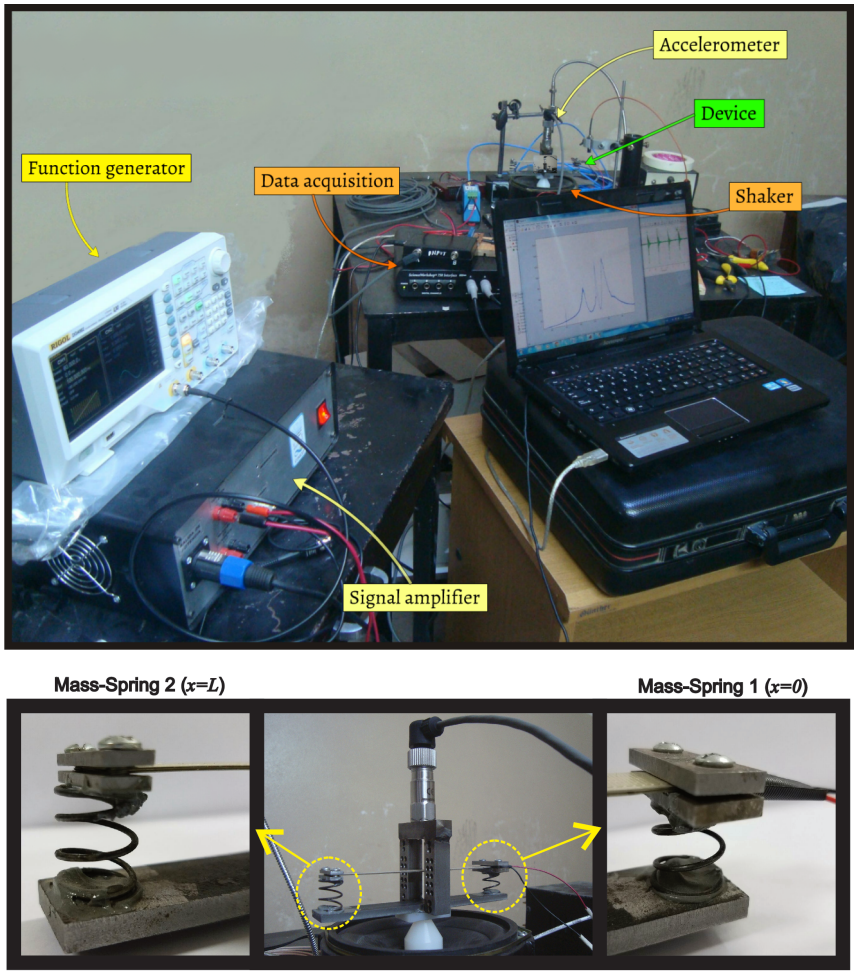

Figure 7. Experimental setup. Top: general scheme. Bottom: detailed view showing the shaker, the device and the accelerometer.

Additionally, the experiments show some additional peaks at around 60 Hz and 75 Hz (first and third modes indicated in Figure 8) that are not predicted by the analytical model. Even though it is not easy to predict the source of these discrepancies, we think that they may be due to some unmodeled effects of the actual harvesting device. Although initially the device was thought to have only vertical displacements, the size of the springs, the amount and distribution of the adhesive layer to bond them to the beam, and the imperfections in the boundary conditions (for example, the joint between the spring and the mass in the beam ends) were not taken into account in the mathematical model and hence do not fit into it.

In order to gain some insight into the source of these differences, we apply Abaqus software to determine the spatial shape in a tridimensional view of the vibration modes. The results are presented in Figure 9, where it is determined that the first peak of the experimental curve (around 60 Hz) corresponds to a lateral (y-direction) vibration mode (Figure 9, left), while the third peak of the same curve (near 75 Hz, Figure 8) corresponds to a first torsional mode of the system (Figure 9, right). As it can be deduced,

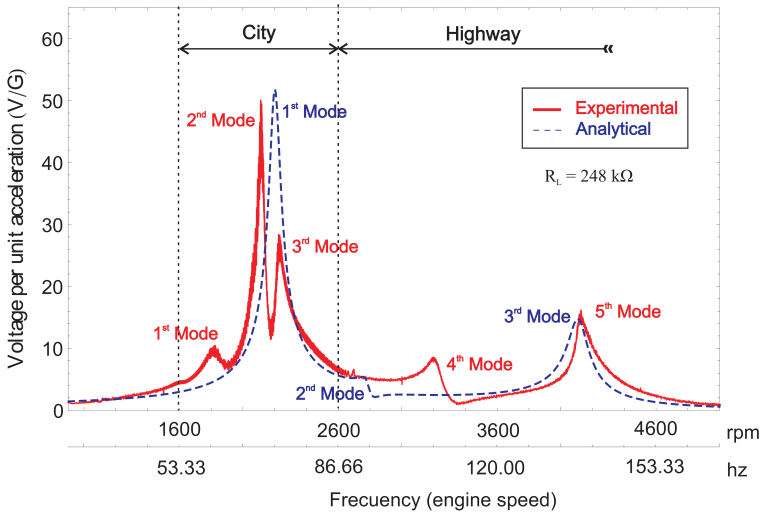

Figure 8. FFT voltage per unit acceleration of gravity in the experimental test for $R_L = 248\,\mathrm{k}\Omega$.

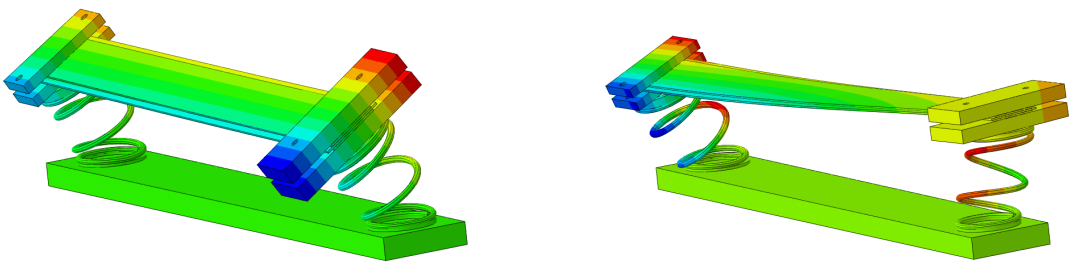

Figure 9. Additional three-dimensional modes generated using Abaqus that were not included in the analytical model. Left: first mode (lateral). Right: third mode (torsional).

it is not possible to analytically predict these additional lateral and torsional modes, and therefore they do not appear in the analytical curve presented in Figure 8. In order to fix this, a more complex model that takes into account the finite size of the springs, for example, must be proposed. However, from an energy harvesting perspective, the presence of these additional modes, although not predicted, enlarges the zone where the device is in resonance or near resonance condition, thus increasing the amount of recovered energy.

Regarding power generation for different acceleration regimes, we use an accelerometer to measure the peak acceleration, shown in Figure 10 (points), as a function of engine rotation velocity (the line represents the tendency). By means of this figure, it is possible to obtain the maximum electrical power — see (37) — for different rotational speeds. For example, at 2200 rpm the acceleration is $2.45G$ (Figure 10), and the maximum generation increases to $51\,\mathrm{V}/G$ (see Figure 8). For a load resistance of $248\,\mathrm{k}\Omega$, this output represents a harvested peak power as large as 63 mW.

It must be noted that a previous work reported a similar device based on an electromagnetic rather than a piezoelectric harvester [Glynne-Jones et al. 2004]. In that approach, a microgenerator of $21\,\mathrm{mm} \times 15\,\mathrm{mm} \times 10\,\mathrm{mm}$ harnessed a peak power of 3.9 mW, representing a power density of nearly $1.25\,\mathrm{mW/cm^3}$.

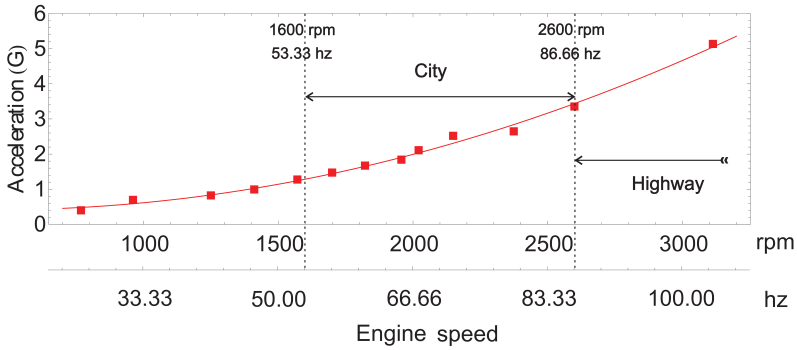

Figure 10. Engine acceleration level based on rpm.

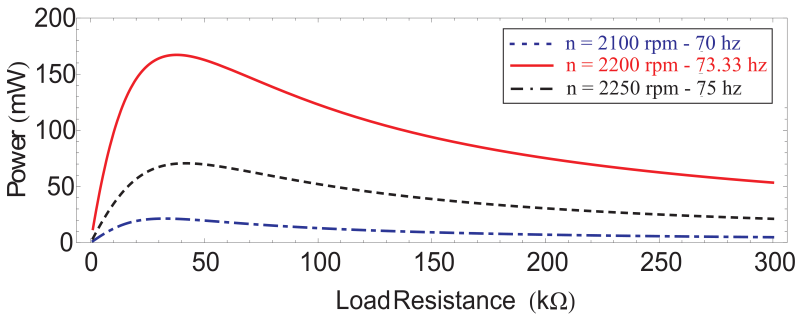

Figure 11. Electrical power as a function of load resistance for each speed measurement.

Our system, on the other hand, collected a power density of 13.5 mW/cm^3, thus obtaining more than ten times as much. This reveals a high power density in the case of the piezoelectric device (our proposal), in agreement with previous findings [Priya 2007].

Finally, the variation in output power with load resistance R_L for different frequencies of engine rotation near the principal resonance is shown in Figure 11. It can be observed that each rotating speed has a single resistance value which maximizes the output power. For example, maximizing the load resistance at 2200 rpm yields a maximum power of 167 mW with a load resistance of 37.8 kΩ. As soon as other frequencies are considered, this maximum value decreases and the same occurs with the optimum resistance, which is a clear indication of the frequency-dependent nature of this value (see for example [Machado et al. 2015]). The same occurs for the rest of the resonances of Figure 8, indicating that a different optimal resistance can be found for those cases. This clearly suggests that the obtained output power values can be improved by an optimization procedure.

Summing up, sufficient analytical and experimental evidence are presented supporting the reliability of the proposed multimodal device to meet the requirements of energy recovery for different speed conditions, both in the city (low speeds) and highway (high speeds, see Figure 8).

5. Conclusions

In this work, an energy harvesting device that can collect energy in a car for different gear ratios is presented. The structural design provides an alternative to the common cantilever beam type of design

to harvest energy in a range of frequencies between 1600 rpm–4600 rpm, which is the range obtained in a drive test with a conventional diesel car. To this end, a piezoelectric energy harvesting device comprising a piezofiber composite with interdigitated electrodes and two mass-spring systems with large flexibility is proposed. The selected PFCB-W14 (from Advanced Cerametrics Inc.) piezobeam seems to be a good choice for both increasing harvesting energy through the use of the piezoelectric constant d_{33} and providing long fatigue life. In the mechanical design, two spring-mass systems at the ends of the beam are included to introduce multiple modes in a frequency that spans the engine's angular velocities. An analytical model based on Lagrangian formulation is developed and solved to predict the dynamic behavior of the system. In a first step towards its validation, ABAQUS software was used to compare the validity of the analytical predictions. The results show that, even though the analytical model predicted most frequencies and modes, a lateral (off-plane) and a torsional mode remained absent in the formulation due to the inability of the model to capture off-plane (vertical) modes.

A set of experiments at different engine speeds was carried out for the proposed system. The results demonstrate good agreement between analytical, computational, and experimental data, showing the accuracy of the models and the relevance of the mechanical design. As for voltage generation over the frequency bandwidth span by engine rotation, a sustained voltage generation over $10\,\mathrm{V}/G$ is reported for the 1600 rpm–2600 rpm range (city journey), with a predicted maximum output power of 63 mW ($51\,\mathrm{V}/G$) at 2200 rpm. For a highway journey (2600 rpm–4600 rpm), the generation is not so large, except in the vicinity of the third/fifth analytical/experimental mode, where voltage grows considerably. Finally an optimization of the load resistance is sketched, demonstrating that these large values can be also increased by a proper optimization procedure. In summary, the proposed harvesting device largely suffices the energy demand to feed low-power automotive sensors. After a comparison with other similar devices, our piezoelectric-based proposal provides a power density solution ten times larger than its electromagnetic counterpart.

Future research should study a delivery method for the harvested power to a storage device in a continuous and stabilized manner by means of AC-DC and DC-DC converters. Finally, the ultimate validation of the model will take place by mounting the device in a car and rolling it down the streets.

Acknowledgments

The authors wish to thank CONICET, ANPCyT, Departamento de Física UNS, and Secretaría de Ciencia y Tecnología UTN-FRBB.

References

[Beckert and Kreher 2003] W. Beckert and W. S. Kreher, "Modelling piezoelectric modules with interdigitated electrode structures", *Comput. Mater. Sci.* **26** (2003), 36–45.

[Bibo and Daqaq 2013] A. Bibo and M. F. Daqaq, "Energy harvesting under combined aerodynamic and base excitations", *J. Sound Vib.* **332**:20 (2013), 5086–5102.

[Bowen et al. 2006] C. R. Bowen, L. J. Nelson, R. Stevens, M. G. Cain, and M. Stewart, "Optimisation of interdigitated electrodes for piezoelectric actuators and active fibre composites", *J. Electroceram.* **16**:4 (2006), 263–269.

[Erturk and Inman 2011] A. Erturk and D. J. Inman, *Piezoelectric energy harvesting*, Wiley, New Delhi, India, 2011.

[Glynne-Jones et al. 2004] P. Glynne-Jones, M. J. Tudor, S. P. Beeby, and N. M. White, "An electromagnetic, vibration-powered generator for intelligent sensor systems", *Sens. Actuators A Phys.* **110** (2004), 344–349.

[Hareesh et al. 2012] P. Hareesh, I. Misri, S. Yang, and D. L. DeVoe, "Transverse interdigitated electrode actuation of homogeneous bulk PZT", *J. Microelectromechanical Sys.* **21**:6 (2012), 1513–1518.

[Harne 2013] R. L. Harne, "Development and testing of a dynamic absorber with corrugated piezoelectric spring for vibration control and energy harvesting applications", *Mech. Syst. Signal Process.* **36**:2 (2013), 604–617.

[Harne and Wang 2013] R. L. Harne and K. W. Wang, "A review of the recent research on vibration energy harvesting via bistable systems", *Smart Mater. Struct.* **22**:2 (2013), 23001–23012.

[He and Gao 2013] X.-F. He and J. Gao, "Wind energy harvesting based on flow-induced-vibration and impact", *Microelectron. Eng.* **111** (2013), 82–86.

[IEE 1988] "IEEE standard on piezoelectricity", IEEE, 1988.

[Kim et al. 2004] H. W. Kim, A. Batra, S. Priya, K. Uchino, D. Markley, R. E. Newnham, and H. F. Hofmann, "Energy harvesting using a piezoelectric "cymbal" transducer in dynamic environment", *Japan. J. Appl. Phys.* **43**:9A (2004), 6178–6183.

[Kim et al. 2006] H. Kim, S. Priya, and K. Uchino, "Modeling of piezoelectric energy harvesting using cymbal transducers", *Japan. J. Appl. Phys.* **45**:7 (2006), 5836–5840.

[Lee et al. 2012] J. Lee, S. Kim, J. Oh, and B. Choi, "A self-powering system based on tire deformation during driving", *I. J. Automot. Technol.* **13**:6 (2012), 963–969.

[Lin and Ding 2013] H. Lin and K. Ding, "A new method for measuring engine rotational speed based on the vibration and discrete spectrum correction technique", *Measurement* **46**:7 (2013), 2056–2064.

[Lin et al. 2013] X.-J. Lin, K.-C. Zhou, X.-Y. Zhang, and D. Zhang, "Development, modeling and application of piezoelectric fiber composites", *Trans. Nonferr. Met. Soc. China* **23**:1 (2013), 98–107.

[Machado et al. 2015] S. P. Machado, M. Febbo, F. Rubio-Marcos, L. A. Ramajo, and M. S. Castro, "Evaluation of the performance of a lead-free piezoelectric material for energy harvesting", *Smart Mater. Struct.* **24**:115011 (2015), 115011, 8 pp.

[Meirovitch and Parker 2010] L. Meirovitch and R. Parker, *Fundamentals of vibrations*, Waveland Press, Long Grove, IL, 2010.

[Mohammad et al. 1995] D. R. A. Mohammad, N. U. Khan, and V. Ramamurti, "On the role of Rayleigh damping", *J. Sound Vib.* **185**:2 (1995), 207–218.

[Nelson et al. 2003] L. J. Nelson, C. R. Bowen, R. Stevens, M. Cain, and M. Stewart, "Modelling and measurement of piezoelectric fibers and interdigitated electrodes for the optimization of piezofibre composites", pp. 556–567 in *Proc. SPIE* (San Diego, California), vol. 5053, 2003.

[Priya 2007] S. Priya, "Advances in energy harvesting using low profile piezoelectric transducers", *J. Electroceram.* **19** (2007), 167–184.

[Ramirez et al. 2017] J. M. Ramirez, C. D. Gatti, S. P. Machado, and M. Febbo, "An experimentally validated finite element formulation for modeling 3D rotational energy harvesters", *Eng. Struct.* **153** (2017), 136–145.

[Rao 2007] S. S. Rao, *Vibration of continuous systems*, Wiley, 2007.

[Ren et al. 2010] B. Ren, S. W. Or, X. Zhao, and H. Luo, "Energy harvesting using a modified rectangular cymbal transducer based on $0.71Pb(Mg_{1/3}Nb_{2/3})O_3$–$0.29PbTiO_3$ single crystal", *J. Appl. Phys.* **107**:034501 (2010).

[Rezaei-Hosseinabadi et al. 2016] N. Rezaei-Hosseinabadi, A. Tabesh, and R. Dehghani, "A topology and design optimization method for wideband piezoelectric wind energy harvesters", *IEEE Trans. Ind. Electron.* **63**:4 (2016), 2165–2173.

[Roundy 2008] S. Roundy, "Energy harvesting for tire pressure monitoring systems: design considerations", pp. 9–12 in *Proc. of PowerMEMS+microEMS* (Sendai, Japan), 2008.

[Sadeqi et al. 2015] S. Sadeqi, S. Arzanpour, and K. H. Hajikolaei, "Broadening the frequency bandwidth of a tire-embedded piezoelectric-based energy harvesting system using coupled linear resonating structure", *IEEE/ASME Trans. Mechatron.* **20**:5 (2015), 2085–2094.

[Shigley 1972] J. E. Shigley, *Mechanical engineering design*, McGraw-Hill, 1972.

[Uchino 1997] K. Uchino, *Piezoelectric actuators and ultrasonic motors*, Kluwer Academic Publishers, 1997.

[Van Blarigan et al. 2015] L. Van Blarigan, J. Moehlis, and R. McMeeking, "Low dimensional modeling of a non-uniform, buckled piezoelectric beam for vibrational energy harvesting", *Smart Mater. Struct.* **24**:6 (2015), 65012–65021.

[Wang et al. 2010] Y.-J. Wang, C.-D. Chen, and C.-K. Sung, "Design of a frequency-adjusting device for harvesting energy from a rotating wheel", *Sens. Actuators A Phys.* **159**:2 (2010), 196–203.

[Wang et al. 2013] Y.-J. Wang, C.-D. Chen, and C.-K. Sung, "System design of a weighted-pendulum-type electromagnetic generator for harvesting energy from a rotating wheel", *IEEE/ASME Trans. Mechatron.* **18**:2 (2013), 754–763.

[Weaver Jr. et al. 1990] W. Weaver Jr., S. P. Timoshenko, and D. H. Young, *Vibration problems in engineering*, Wiley, 1990.

[Xiao and Wang 2014] H. Xiao and X. Wang, "A review of piezoelectric vibration energy harvesting techniques", *International Review of Mechanical Engineering* (*IREME*) **8**:3 (2014), 609–620.

[Xu et al. 2013] T.-B. Xu, E. J. Siochi, J. H. Kang, L. Zuo, W. Zhou, X. Tang, and X. Jiang, "Energy harvesting using a PZT ceramic multilayer stack", *Smart Mater. Struct.* **22**:6 (2013), 65015–65029.

[Zhang et al. 2007] Y. Zhang, K. Huang, F. Yu, Y. Gu, and D. Li, "Experimental verification of energy-regenerative feasibility for an automotive electrical suspension system", pp. 1–5 in *IEEE Int. Conf. Veh. Electronics and Safety*, 2007.

[Zhang et al. 2012] G. Zhang, J. Cao, and F. Yu, "Design of active and energy-regenerative controllers for DC-motor-based suspension", *Mechatronics* **22**:8 (2012), 1124–1134.

[Zhu et al. 2010] D. Zhu, M. J. Tudor, and S. P. Beeby, "Strategies for increasing the operating frequency range of vibration energy harvesters: a review", *Measurement Sci. Technol.* **21**:2 (2010), 22001–22029.

[Zuo and Zhang 2013] L. Zuo and P.-S. Zhang, "Energy harvesting, ride comfort, and road handling of regenerative vehicle suspensions", *J. Vib. Acoust.* (*ASME*) **135**:1 (2013), 110021–110028.

Received 24 May 2017. Revised 19 Oct 2017. Accepted 20 Nov 2017.

CLAUDIO D. GATTI: cdgatti@frbb.utn.edu.ar
Grupo de Investigación en Multifísica Aplicada (GIMAP), Universidad Tecnológica Nacional, Bahía Blanca, Argentina

JOSÉ M. RAMIREZ: josemramire@gmail.com
Grupo de Investigación en Multifísica Aplicada (GIMAP), Universidad Tecnológica Nacional, Bahía Blanca, Argentina

MARIANO FEBBO: mfebbo@uns.edu.ar
Instituto de Física del Sur (IFISUR) and Departamento de Física, Universidad Nacional del Sur, Bahía Blanca, Argentina

SEBASTIÁN P. MACHADO: smachado@frbb.utn.edu.ar
Grupo de Investigación en Multifísica Aplicada (GIMAP), Universidad Tecnológica Nacional, Bahía Blanca, Argentina